

Contents lists available at ScienceDirect

#### Petroleum Science

journal homepage: www.keaipublishing.com/en/journals/petroleum-science



#### Original Paper

### Evolution of the 3D pore structure of organic-rich shale with temperature based on micro-nano CT



Chao-Fan Zhu <sup>a, b, c, d</sup>, Tian-Le Zhang <sup>a, b, c, d</sup>, Jun-Fan Pan <sup>a, b, c, d</sup>, Yan-Wei Li <sup>a, b, c, d</sup>, James J. Sheng <sup>e</sup>, Dong Ge <sup>a, b, c, d</sup>, Rui Jia <sup>a, b, c, d, \*</sup>, Wei Guo <sup>a, b, c, d, \*\*</sup>

- a College of Construction Engineering, Jilin University, State Key Laboratory of Deep Earth Exploration and Imaging, Changchun, 130026, Jilin, China
- b National-Local Joint Engineering Laboratory of In-situ Conversion, Drilling and Exploitation Technology for Oil Shale, Changchun, 130021, Jilin, China
- <sup>c</sup> Provincial and Ministerial Co-construction of Collaborative Innovation Center for Shale Oil & Gas Exploration and Development, Jilin University, Changchun, 130021, Jilin, China
- d Key Lab of Ministry of Natural Resources for Drilling and Exploitation Technology in Complex Conditions, Jilin University, Changchun, 130021, Jilin, China
- e College of Petroleum Engineering, North East Petroleum University, Daqing, 066004, Heilongjiang, China

#### ARTICLE INFO

# Article history: Received 31 October 2024 Received in revised form 19 January 2025 Accepted 24 March 2025 Available online 29 March 2025

Edited by Meng-Jiao Zhou

Keywords:
Organic-rich shale
Micro-nano CT
Kerogen
Pores
Pyrolysis

#### ABSTRACT

Organic-rich shale is a significant potential source of oil and gas that requires development through in situ conversion technology. However, the evolution patterns of the internal three-dimensional (3D) pore structure and kerogen distribution at high temperatures are not well understood, making it difficult to microscopically explain the evolution of the flow conductivity in organic-rich shale at high temperatures. This study utilizes high-resolution X-ray computed tomography (micro-nano CT) to obtain the distribution of pores, kerogen, and inorganic matter at different temperatures. Combined with the pyrolysis results for the rock, the evolution of the pore structure at various temperatures is quantitatively analyzed. Based on three-phase segmentation technology, a model of kerogen distribution in organic-rich shale is established by dividing the kerogen into clustered kerogen and dispersed kerogen stored in the inorganic matter and the pores into inorganic pores and organic pores within the kerogen skeleton.

The results show that the inorganic pores in organic-rich shale evolve through three stages as the temperature increases: kerogen pyrolysis (200–400 °C), clay mineral decomposition (400–600 °C), and carbonate mineral decomposition (600–800 °C). The inorganic pores porosity sequentially increases from 3% to 11.4%, 13.1%, and 15.4%, and the roughness and connectivity of the inorganic pores gradually increase during this process. When the pyrolysis temperature reaches 400 °C, the volume of clustered kerogen decreases from 25% to 12.5%. During this process, the relative density of kerogen decreases from 9.5 g/cm³ in its original state to 5.4 g/cm³, while the kerogen skeleton density increases from 1.15 g/cm³ in its original state to 1.54 g/cm³. Correspondingly, 7%–8% of organic pores develop within the clustered kerogen, accounting for approximately 50% of the volume of clustered kerogen. In addition, approximately 30% of the kerogen in organic-rich shale exists in the form of dispersed kerogen within inorganic matter, and its variation trend is similar to that of clustered kerogen, rapidly decreasing from 200 to 400 °C and stabilizing above 400 °C. The results of this study provide an essential microscopic theoretical basis for the industrial development of organic-rich shale resources.

© 2025 The Authors. Publishing services by Elsevier B.V. on behalf of KeAi Communications Co. Ltd. This is an open access article under the CC BY-NC-ND license (http://creativecommons.org/licenses/by-nc-nd/4.0/).

#### 1. Introduction

As technology rapidly advances, energy issues have become barriers to the rapid development of global productivity. The traditional energy industry is committed to exploring new methods of obtaining energy (Na et al., 2012; Hu et al., 2022; Li et al., 2022). Organic-rich shale, which is a widely distributed and globally

E-mail addresses: jiarui@jlu.edu.cn (R. Jia), guowei6981@jlu.edu.cn (W. Guo).

<sup>\*</sup> Corresponding author.

<sup>\*\*</sup> Corresponding author.

abundant unconventional energy resource (Qian et al., 2006; Knaus et al., 2010; Niu et al., 2013; Han et al., 2014), is a potential source of oil and gas. In China, organic-rich shale reserves are abundant (Liu et al., 2006; Wang et al., 2012; Zou et al., 2012), with proven reserves reaching trillions of barrels. However, the difficulty and high cost of extraction mean that large-scale development still requires disruptive technological support (Liu and Liu, 2005).

Organic-rich shale is a heterogeneous, dense, sedimentary rock that is rich in organic matter (Sun et al., 2014). It has a very low original porosity comprising mostly micropores and mesopores with poor connectivity, resulting in very low permeability and posing significant challenges for hydrocarbon extraction (Liu et al., 2023). To address these challenges, in situ pyrolysis is internationally recognized as a promising method of exploitation (Kang et al., 2020; Zhao and Kang, 2020; Guo et al., 2022, 2023; Yang et al., 2023), and this method involves heating underground organic-rich shale reservoirs to induce the thermal decomposition of kerogen into oil and gas, which can greatly improve the transport capacity of organic-rich shale.

Inorganic matter (IOM) develops secondary pores and fractures during in-situ high-temperature pyrolysis. Meanwhile, kerogen pyrolysis not only generates oil and gas but also forms numerous organic pores (OP). These newly formed pore structures constitute multi-scale storage spaces, providing effective pathways for hydrocarbon migration and thus enhancing the transport capacity of organic-rich shale to some extent. Given the pivotal role of the internal pore structure of organic-rich shale in hydrocarbon resource development and pyrolysis processes, accurate and indepth quantitative and qualitative characterization of it is of great importance. This helps us comprehensively understand the characteristics of organic-rich shale reservoirs, providing a solid scientific basis for reservoir development and revealing the deep mysteries of organic-rich shale pyrolysis mechanisms, offering powerful theoretical support for optimizing pyrolysis processes and increasing hydrocarbon production.

Micro-computed tomography (micro-CT) offers non-destructively high-resolution imaging of specimen microstructures (Kang et al., 2017; Zou and Sun, 2020). It has been widely used to study the internal structure of organic-rich shales (Tiwari et al., 2013; Rabbani et al., 2017; Saif et al., 2019; Lin et al., 2022; Zhan et al., 2022). However, these studies overlooked the characterization of kerogen, a crucial component in organic-rich shale. Huang et al. (2021) proposed a three-phase segmentation method based on the traditional two-phase segmentation approach (segmenting data images into pores, kerogen, and matrix) to analyze changes in kerogen content during the pyrolysis of organic-rich shale. Yet, they did not conduct further research on kerogen.

Some studies indicated that as pyrolysis progresses, a considerable amount of kerogen residue persists in organic-rich shale, and numerous nanoscale pores develop within this kerogen (Saif et al., 2017; Lei et al., 2021). However, due to the current limitations in CT technology precision, even the most advanced CT equipment cannot accurately capture these OP structures within kerogen. Consequently, in previous CT studies, kerogen was often simplified as a compact solid phase, and the evolution of its internal pores was severely neglected. Furthermore, these studies primarily focused on kerogen clusters that CT technology could identify while lacking sufficient attention to the fine and dispersed kerogen (DK) within clay intercalations.

This study establishes a model and characterization method for the distribution of kerogen and pores in organic-rich shales. Based on traditional three-phase segmentation, kerogen in the organicrich shale is divided into clustered kerogen (CK) and DK, and the pores are divided into IOP and OP. CT can directly determine the CK and IOP, whereas the OP in the CK and DK in the IOM need to be quantitatively obtained by combining rock pyrolysis analysis with the density of the KS. This method is used to systematically study the evolution of the pore structure during the pyrolysis of organicrich shale.

#### 2. Materials and methods

#### 2.1. Organic-rich shale specimens

In this study, organic-rich shale specimens were carefully selected from the Huadian deposit in the Songliao Basin of Jilin Province. The organic-rich shale from the Huadian Basin presents a spectrum of colors, including gray-brown, brownish-gray, and black, with a dense, blocky texture and a characteristic shell-like fracture. It leaves a brown streak when rubbed and can be ignited with a naked flame, indicating its rich organic content. The rock is replete with various fossilized remains of both plant and animal origins as well as plant debris (Wang et al., 2005).

The organic-rich shale in the Huadian Basin is found at relatively shallow depths, ranging from 0 to 500 m, and is celebrated for its high oil yield of between 8% and 13%. It also exhibits a commendably low ash yield, ranging from 52.97% to 62.10%. These characteristics categorize it as a superior-quality organic-rich shale deposit (Wang et al., 2005), particularly in the industrial context. It is recognized for its low ash and high oil content, which endow it with substantial value for development and utilization.

The principal minerals in the Huadian organic-rich shale include quartz, dolomite, illite—smectite mixed layers (I/S), calcite, and pyrite. Notably, clay minerals such as illite, and I/S are found in higher concentrations. Details of the mineral composition are presented in Table 1, which provides a comprehensive accounting of the constituents of the organic-rich shale.

To minimize the influence of the inherent heterogeneity of the organic-rich shale on the pyrolysis experiments and CT scanning, the specimens for this study were carefully selected from a uniform stratum within a single organic-rich shale block. The specimens were then processed into granules with a mesh size of 10–20, providing a standardized form for the experiments.

The granulated organic-rich shale specimens were carefully separated into seven equal groups of 40 ( $\pm$ 0.1) g to ensure consistency across all experimental conditions. Each group was subjected to a controlled drying process in an oven maintained at 80 °C for 12 h

Following the drying process, the specimens were sealed in individual bags to maintain their integrity and prevent environmental factors from affecting their composition before the experiments. This rigorous preparation protocol was critical to ensure the reliability and reproducibility of the outcomes of both the pyrolysis experiments and the CT scanning analysis.

## 2.2. Distillation experiments with organic-rich shale at different temperatures

The experimental setup and procedure for pyrolysis, as depicted in Fig. 1, were described in our previous research (Xu et al., 2021). First, the gas tightness of the apparatus was evaluated to ensure its integrity. Once the apparatus was confirmed to have good gas tightness, 40 g of raw organic-rich shale was placed on a metal wire mesh in a quartz distillation flask (inner diameter: 50 mm, height: 140 mm). The metal wire mesh ensured complete contact between the organic-rich shale and nitrogen during pyrolysis.

Nitrogen was introduced to the reaction vessel for 30 min to ensure a pure reaction atmosphere. Subsequently, the shale specimen was heated externally at  $10\,^{\circ}$ C/min from ambient temperature (23  $^{\circ}$ C) to target temperatures of 200, 300, 400, 500, 600, 700, and

**Table 1**Mineral composition of organic-rich shale.

Mineral composition	Quartz	Calcite	Dolomite	Chlorite	Illite	I/S	Others
Content, %	7.36	10.82	0.25	2.31	0.21	76.2	2.85

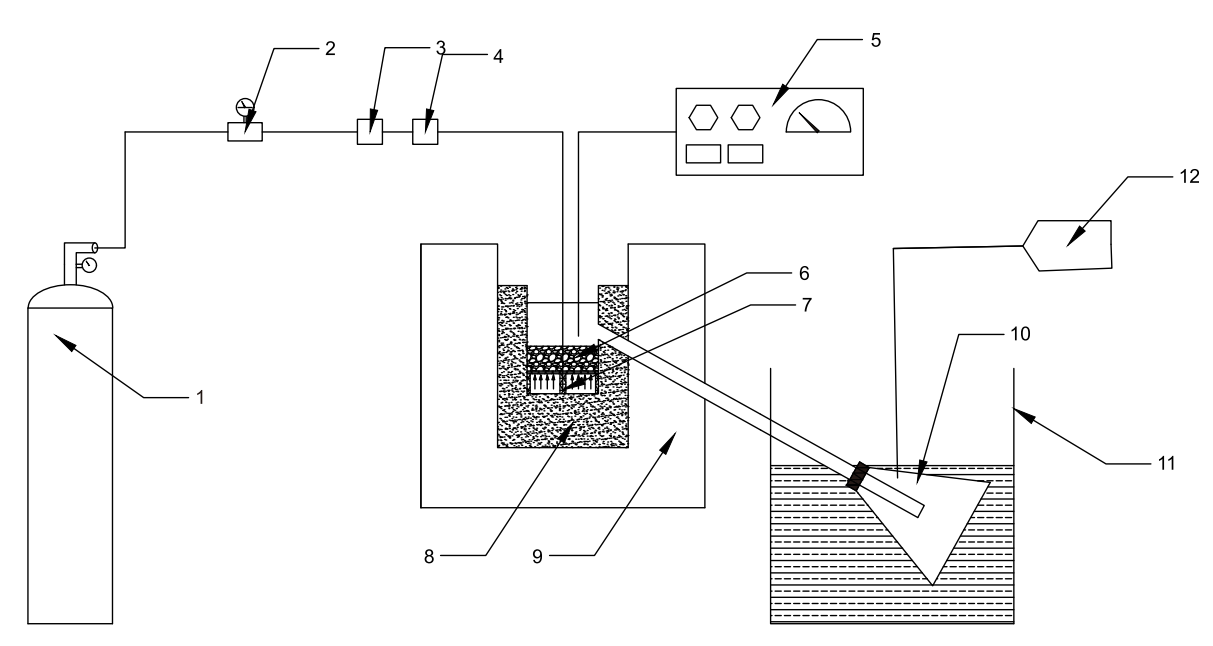


**Fig. 1.** Schematic diagram of the experimental device (1: N<sub>2</sub> cylinder; 2: pressure gauge; 3: mass flowmeter; 4: flow controller; 5: temperature control panel; 6: specimen; 7: metal mesh; 8: thermal insulation cotton; 9: furnace; 10: conical bottle; 11: condenser; 12: gas collection bag).

 $800\,^{\circ}$ C. Upon reaching the desired temperature, the specimens were held for 2 h to ensure a complete reaction of the kerogen within the organic-rich shale at the given temperature. After the distillation experiment was completed, the samples were naturally cooled to room temperature and collected for subsequent CT scanning experiments.

During the experiment, a thermocouple was used to monitor and maintain the external temperature of the specimen. The internal temperature varied owing to the high-temperature decomposition of kerogen, self-heating effects, and other reactions. The nitrogen flow rate was maintained at 80 mL/min throughout all experiments using a flow control device. The specimens were labeled according to their final pyrolysis temperatures as N-200, N-300, N-400, N-500, N-600, N-700, and N-800. High-purity nitrogen was used in the process.

The weight changes of the specimens were recorded throughout the experiment, as shown in Fig. 2.

The original volume of the specimen obtained in the drainage experiment was 24.24 cm<sup>3</sup>. Assuming that the volume of the specimens remained unchanged during the pyrolysis process, their densities were calculated as summarized in Table 2.

#### 2.3. Rock pyrolysis experiments

The experimental apparatus used is an OG-2000V rock pyrolysis instrument (Oil and Gas Display Evaluation Apparatus) produced by Shandong Jinpu Analysis Co., Ltd. (Fig. 3). This equipment is an oil and gas display evaluation instrument developed following the GB/T18602-2012 standard for oil fields, coal mines, geological exploration, coalbed methane, and shale gas development. It performs the functions of rock pyrolysis and analysis of the residual

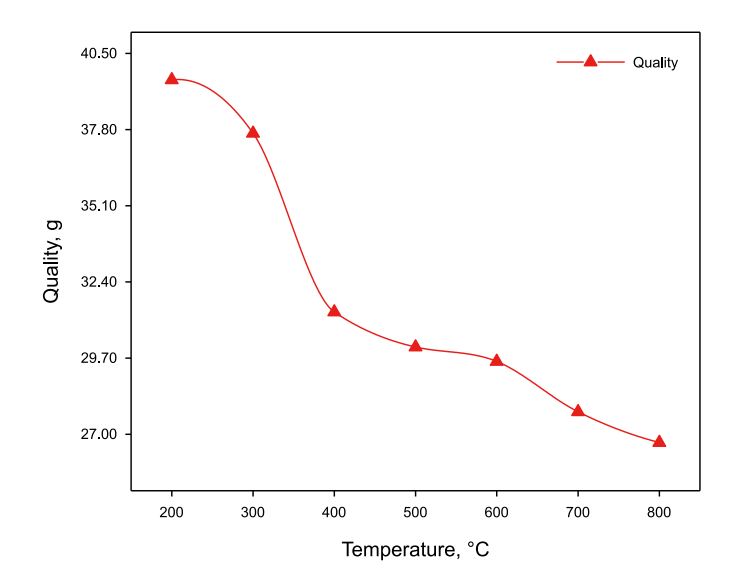


Fig. 2. Change in specimen quality during dry distillation.

**Table 2**Specimen densities.

Specimen	N-200	N-300	N-400	N-500	N-600	N-700	N-800
Density, g/cm <sup>3</sup>	1.63	1.55	1.29	1.24	1.22	1.15	1.10

carbon content.

The operational procedures and experimental materials



Fig. 3. Rock pyrolizer.

followed the national standard (GB/T18602-2012), with measured parameters comprising the content of residual hydrocarbons, pyrolytic hydrocarbons, CO<sub>2</sub> generated by pyrolysis, and residual organic carbon produced by pyrolysis. The content of hydrocarbons in the specimens is listed in Table 3.

$$M_k = S_1 + S_2 + S_3 + S_4^{CO} \cdot C_m / CO_m + S_4^{CO_2} \cdot C_m / CO_{2m}$$
 (1)

In Eq. (1),  $M_k$  is the Organic matter content, mg/g,  $S_1$  is the residual hydrocarbon content, mg/g,  $S_2$  is the content of cracked hydrocarbon, mg/g,  $S_3$  is the  $CO_2$  produced by pyrolysis, mg/g,  $S_4$  is the residual organic carbon after pyrolysis, mg/g (which can be divided into two forms: CO and  $CO_2$ ),  $C_m$  is the molecular weight of carbon,  $Co_m$  is the molecular weight of carbon monoxide, and  $CO_{2m}$  is the molecular weight of carbon dioxide.

The pyrolysis results indicate that the Huadian organic-rich shale has a minimal content of residual hydrocarbons ( $S_1$ ), with the oil and gas predominantly present as pyrolytic hydrocarbons ( $S_2$ ). These pyrolytic hydrocarbons undergo a minor degree of pyrolysis between 200 and 300 °C, with the principal pyrolysis taking place in the temperature range of 300–400 °C. Above 400 °C, the pyrolysis of  $S_2$  is sufficient. After pyrolysis, the organic matter is primarily residual in the form of  $S_4$ . The residual content of  $S_4$  after the thermal decomposition of organic matter is substantial, constituting 36.5% of the total organic matter mass. The content of each component remains stable after pyrolysis at 500 °C, indicating that the organic matter has undergone sufficient pyrolysis at 500 °C. Beyond 500 °C, organic matter primarily exists in the form of residual carbon.

**Table 3**Rock pyrolysis results.

Specimen	S <sub>1</sub> , mg/g	S <sub>2</sub> , mg/g	S <sub>3</sub> , mg/g	S <sub>4</sub> <sup>CO</sup> , mg/g	$S_4^{\text{CO}_2}$ , mg/g
N-200	0.67	135.12	5.14	26.09	255.82
N-300	0.92	112.76	3.75	36.50	256.94
N-400	0.66	1.51	2.42	36.51	227.19
N-500	0.57	0.47	1.63	37.75	241.81
N-600	0.38	0.25	1.09	38.27	240.81
N-700	0.48	0.27	0.99	38.42	241.36
N-800	0.35	0.44	0.40	37.81	241.41

#### 2.4. Micro-nano CT scanning and image analysis

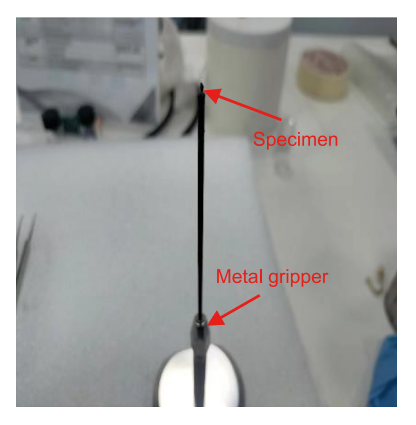
#### 2.4.1. Micro-nano CT scanning

During the micro-CT scanning experiment, the samples used were derived from the organic-rich shale semi-coke after the distillation process. Due to the limitations of the flat panel detector in the CT equipment, the size of the samples was strictly controlled to a width of approximately 0.5 mm and a length of 1 mm to ensure high-resolution data and maximize the imaging range. The scanning experiment was conducted under ambient temperature and pressure conditions.

The experimental procedure employs a Sanying nanovoxel-5000 series micro-CT scanner, which is a state-of-the-art imaging tool that facilitates non-destructive, high-resolution 3D visualization of specimens. Specimens were fixed onto a metallic clamping device which is affixed to a rotational stage through a ball-and-socket joint (Fig. 4). Illuminated by a micro-focus X-ray source, the X-rays traverse the specimen to capture density information that is projected onto a detector. The photosensitive components of the detector transform this information into visual data. Acquisition of images from multiple angles generates a composite 3D image through software reconstruction. The scanner maintains a high pixel resolution and delivers accurate quantitative analysis.

The pixel detail resolution shows the physical dimension represented by a single pixel in the CT image, whereas the spatial resolution represents the ability of the scanner to discern minor distinguishable geometric details within the image. The imaging area is an expansion of the photosensitive region of the detector, and the pixel matrix represents the density of these photosensitive points. Detailed specifications of the CT scanner are listed in Table 4.

When executing scanning tasks, several parameters are of particular importance, including the voltage, current, source-to-object distance (SOD), source-to-detector distance (SDD), exposure time, image merge count, and scan frame number. These parameters are crucial for optimizing the scanning process to achieve the desired image quality and resolution. The scanning parameters



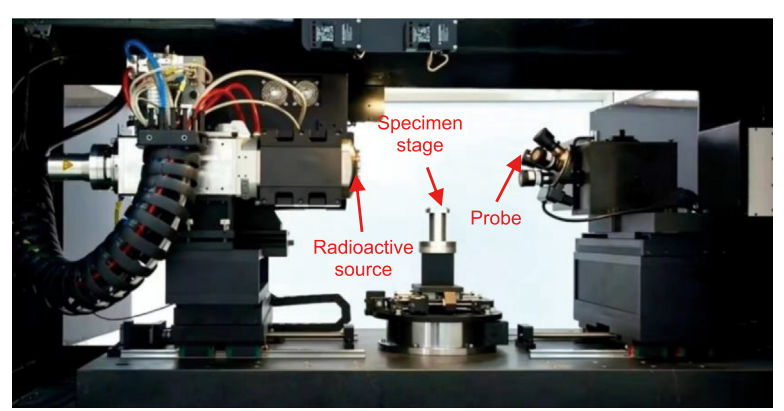


Fig. 4. Specimen and equipment interior photos.

**Table 4** Device-dependent parameters.

Resolution	Pixel detail resolution	200 nm
	Spatial resolution	500 nm
X-ray source	Type	Open tube transmission (microfocus/nanofocus)
	Maximum voltage	240 kV/160 kV
Flat panel detector	Imaging area	427 mm × 427 mm
	Pixel matrix	$3072 \times 3072$
Specimen	Specimen size that can be detected	$600 \text{ mm} \times 600 \text{ mm}$
	Specimen bearing	25 kg/100 kg
Physical parameters of equipment	Equipment size	2770 mm × 1540 mm × 2040 mm
- · ·	Equipment weight	4500 kg/8000 kg

used in this study are listed in Table 5. A monochromatic X-ray beam energy of 60 kV was used with the beam filtered by Aluminum filters. The exposure time for projection was 16 s and there were 1440 projections in total for each scan with a field of view of 0.88 mm  $\times$  0.62 mm, The acquisition time for each scan was 4 s with a completed voxel size of 0.35  $\times$  0.35  $\times$  0.35  $\mu m^3$ . The sample was positioned 2.73 mm away from the X-ray source and 380 mm away from the flat panel detector.

The voltage level determines the penetration power of the X-rays. The higher the voltage, the greater the penetrating ability will be. Because the specimens in this study are small and have relatively low density, a lower voltage setting is selected to extract sufficient material information. The current level dictates the output power of the X-rays; the exposure time is the duration of irradiation required for each two-dimensional projection image. The longer the exposure time, the more precise the digital radiography (DR) image will be. The image merge count indicates the number of images combined to form a single DR image. The higher the image merge count, the longer the irradiation time and the higher the image precision will be. The scan frame number refers to the quantity of images output as the specimen rotates by 360°. The higher the scan frame number, the greater the image precision will be.

In terms of image reconstruction, this experiment used the Voxel Studio Recon software, employing cutting-edge techniques such as the Filtered Back Projection (FBP) algorithm and Iterative Reconstruction Algorithms (IRA) to efficiently process twodimensional projection data. Subsequently, precise corrections and optimizations were implemented to obtain high-quality 3D data, effectively mitigating beam hardening effects and enhancing image clarity. To address potential misalignments between the sedimentary bedding plane of the organic-rich shale and the coordinate plane, a coordinate transformation was executed, aligning the sedimentary bedding plane of the organic-rich shale digital core perpendicular to the XOY plane of the three-dimensional coordinate system. To enable comparisons among diverse samples, we randomly selected four cubic volumes, each measuring  $700 \times 700 \times 700$  voxels, from each 3D CT image of the organic-rich shale cores for detailed analysis.

In this study, there is a limitation in the experimental design that may affect the universality and interpretability of our results. The samples used in the scanning experiments were cooled to room temperature before scanning. There are inevitable differences in pore structure characteristics between these samples and those under high-temperature conditions. Although some studies (Lu et al., 2023) on thermal damage to shale under high temperatures indicate that the natural cooling method used in this study has

minimal impact on the structure of the shale sample, the differences require further investigation.

#### 2.4.2. CT image analysis

This study employed the Avizo software to process the original grayscale CT images with 16-bit unsigned binary data. The segmentation method is based on a three-phase segmentation (Huang et al., 2021), dividing the specimen images into inorganic matter, organic matter, and pores, which correspond to IOM, CK, and IOP in this study. The primary basis for segmentation is the grayscale gradient of the CT images (Fig. 5). The intensity of the gray values in CT images is directly related to the material density, with higher gray values (which appear brighter in the images) indicating higher material density. Therefore, theoretically, a reasonable selection of the gray value threshold can allow for the separation of components with different densities in the grayscale images. The specific operations of the three-phase segmentation method are as follows.

- (1) Binarize the original grayscale CT image based on the Interactive Thresholding module. By adjusting the parameter (where the parameter adopted is associated with the grayscale of the pixels) of the module ports, an appropriate threshold was searched to separate the foreground (target) from the background, thereby achieving image binarization. In the binarized image, colorless regions represent areas of no interest and are assigned a value of 0, while colored regions represent regions of interest and are assigned a value of 1. This step preliminarily distinguishes pores and CK based on grayscale gradients.
- (2) Binarize the original CT grayscale image based on the Black Top-Hat Transform method. This method works by performing a closing operation, which includes dilation followed by erosion, to expand bright areas and fill gaps. This makes the bright regions more continuous. Then, the original image is subtracted from the closed image. The subtraction highlights changes in dark areas, such as shadows or low-reflectance regions, making them more prominent and easier to analyze. The Kernel size decides the dimensions of the convolution filter. In the process of binarization in this paper, the Kernel size is 13 × 13. It determines the extent of the area over which the operation is applied. This step can extract small pores that are not obvious in the image.
- (3) Overlay the large pores obtained in step (1) with the small pores obtained in step (2) and calculate the new gray value of the image at each pixel according to the principle 0+0=0, 0+1=1, and 1+1=1. Through this step, IOP can be finally identified.

**Table 5**Key CT scanning parameters.

V, kV	I, A	SOD, mm	SDD, mm	Exposure time, s	Image merge number	Scan frame count
60	1.5	2.73	380	4	4	1440

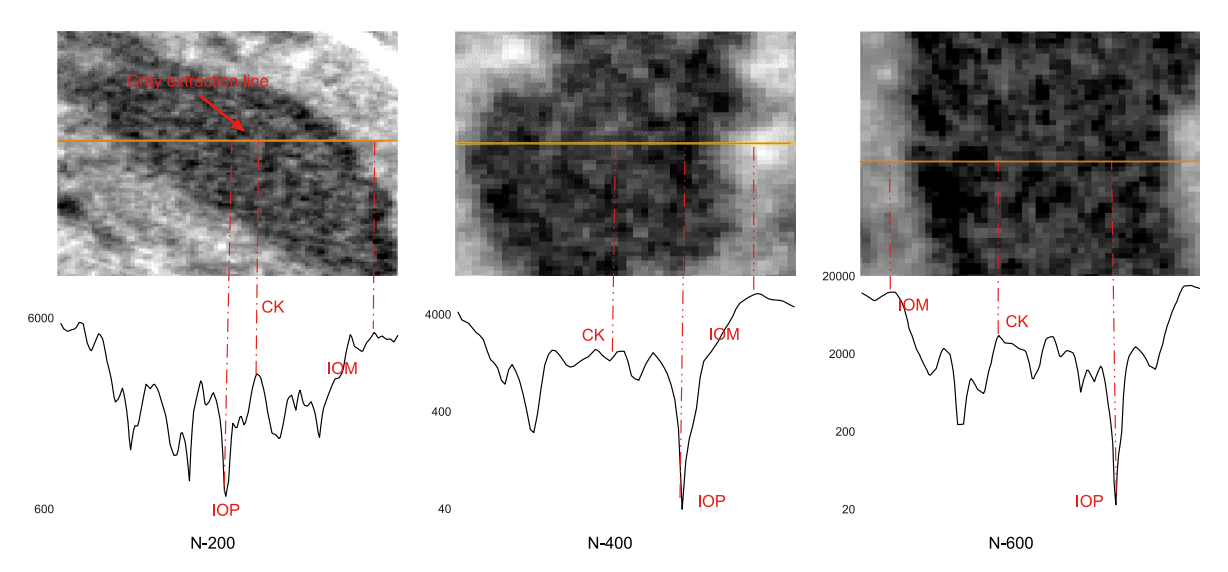


Fig. 5. CT local grayscale image.

It is important to emphasize that the rays passing through the pores are partially absorbed by the pore walls owing to the absorption of X-rays by high-density materials. This property significantly affects small pores, leading to a higher grayscale value for small pores. Therefore, based on traditional threshold segmentation, a local brightness difference segmentation method is used, which extracts small pores based on the grayscale difference of the local image.

#### 3. Results and discussion

#### 3.1. IOP characterization

#### 3.1.1. Three-dimensional characterization of IOP

Temperature significantly influences the evolution of pores and fractures in organic-rich shales; these pores and fractures serve as the primary conduit for the migration of kerogen pyrolysis products. When high-temperature nitrogen gas is used as a heat carrier for in situ heating of organic-rich shale, its ability to penetrate the rock directly affects the allowable heating range and the oil and gas conversion rate. Fig. 6 illustrates the distribution of pores and fractures within the organic-rich shale, showing a microscopic three-dimensional model of the pores. At 200 °C, the organic-rich shale contains relatively few pore structures, with a minor proportion of pores mainly consisting of fractures developed along the bedding planes (accounting for 40% of the IOP). The pores in CK develop significantly at a pyrolysis temperature of 300 °C, forming the central part of the IOP structure. At a pyrolysis temperature of 400 °C, a large number of secondary fractures appear in the organic-rich shale owing to thermal stress (occupying 7.9% of the total volume); these secondary fractures are primarily distributed along the bedding planes and connect the pores and fractures caused by CK pyrolysis, thus greatly expanding the reach of hightemperature gases. After pyrolysis at 500 °C, the fractures expand (occupying 9.3% of the total volume), and the number of small pores decreases (down 22% from N-400). According to a study by Sun (Sun, 2013; Wang et al., 2013), when the retorting temperature exceeds 500 °C, the clay minerals in the organic-rich shale (such as kaolinite) will begin to pyrolyze, and the layered structure of the clay minerals will deteriorate, resulting in a reduction in the pore bedding structure. When the retorting temperature reaches 800 °C, the layered structure is further reduced, and the study indicated

that carbonate minerals will pyrolyze extensively after heating to 800 °C (Sun, 2013; Wang et al., 2013), causing the pore structure to collapse and the bedding structure to weaken further.

Fig. 7 illustrates the trend in the IOP content in the organic-rich shale during the heating process. The IOP in the organic-rich shale mainly exhibits an increasing trend during pyrolysis, which can be divided into two stages. From 300 to 400 °C, the kerogen in the organic-rich shale begins to pyrolyze, leading to changes in the pore structure. When the temperature exceeds 400 °C, the main factors increasing the IOP porosity are cracking along the bedding surface and the decomposition of inorganic minerals.

#### 3.1.2. Pore size distribution

To further explore and quantify the evolution of the pore structure during the pyrolysis of organic-rich shale, the equivalent diameter and volume parameters of the pores are extracted and plotted as pore volume growth curves. Differentiating the growth curves yields the pore size distribution. Fig. 8 illustrates the pore volume growth curves and pore size distribution for the IOP. Because the pixel precision used in this study is  $0.35\times0.35\times0.35~\mu\text{m}^3$  (equivalent diameter of  $0.434~\mu\text{m}$ ), the pore size analysis in Fig. 8 started from  $0.434~\mu\text{m}$  (434 nm).

Visual analysis reveals that the progression of the IOP volume appears to be bifurcated at 10  $\mu m$ , delineating two distinct phases. This demarcation is mirrored in the pore size distribution graph, which exhibits two pronounced peaks. The positioning of these peaks corresponds to the most probable pore diameters, indicating the pore size range with the highest frequency of occurrence, and thus the characteristic pore diameters. The amplitudes of these peaks indicate the relative abundance of pores.

As shown in Fig. 8, specimen N-200 is predominantly characterized by small pores. Upon pyrolysis at 300  $^{\circ}$ C, a noticeable increase in the quantity of small pores occurs, concomitant with an enlargement in the pore dimensions. At 400  $^{\circ}$ C, the prevalence of small pores reaches a peak, and the emergence of a novel peak at 50  $\mu$ m indicates a substantial proliferation of pores and fractures.

As the temperature increases to  $500\,^{\circ}$ C, a noticeable increase in the number of larger pores is observed, while the peak shifts forward. This shift indicates a decrease in the average pore diameter, suggesting that the large pores within the specimen have reached a mature state and with their sizes have reached their maximum extent.

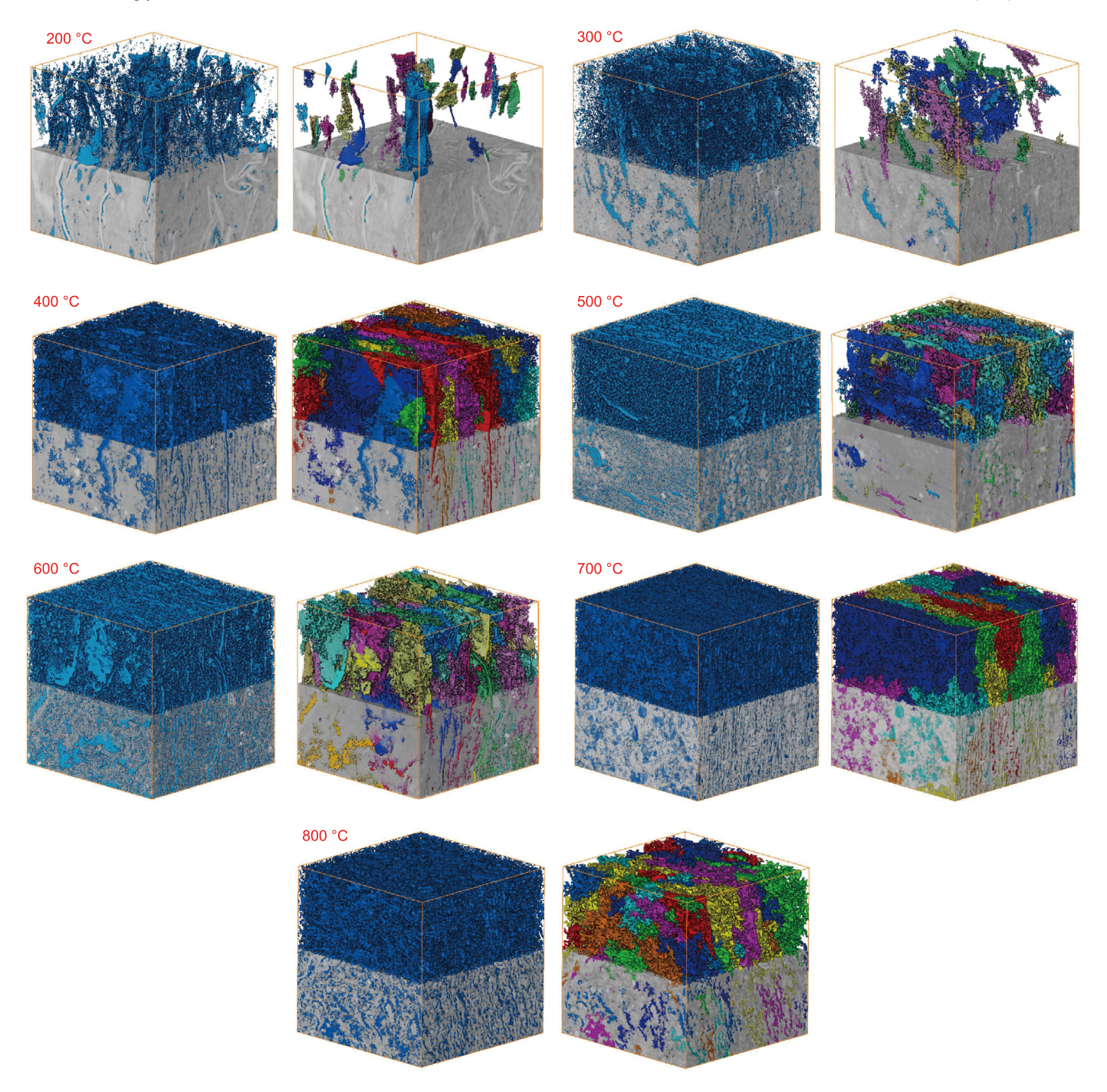


Fig. 6. 3-D volume rendered image with the IOP shown in blue and fractures shown in colors (CT data dimensions:  $700 \times 700 \times 700$  pixels, with a pixel size of  $0.35 \ \mu m \times 0.35 \ \mu m \times 0.35 \ \mu m$ ).

Between 500 and 600 °C, the pyrolysis of clay minerals leads to the collapse of the stratified structure, resulting in a decrease in the most probable pore diameter. This phase is marked by an enhanced interconnectedness among small pores, with their relative quantity gradually decreasing as the temperature increases. Beyond 700 °C, the anterior shift in the small pore peak implies these pores have converged into more expansive voids.

At 800  $^{\circ}$ C, the thermal decomposition of carbonate minerals in the organic-rich shale specimen leads to a further anterior shift in the peak position on the curve, highlighting temperature-induced changes in the pore structure dynamics.

#### 3.1.3. Fractal dimension

The three-dimensional fractal dimension serves as a crucial indicator for evaluating the complexity of pore structures in organic-rich shale. It reflects the roughness of pore surfaces and their spatial filling capacity, which is vital for understanding reservoir permeability and oil/gas storage potential. Analysis of the fractal dimension enables guiding reservoir evaluation and optimization of block development plans. In this study, fractal theory is utilized to describe the geometric structure of pores at different pyrolysis temperatures. The three-dimensional fractal dimension lies between 2 (exclusive) and 3 (inclusive), and the rougher the geometric surface of the structure, the closer the fractal dimension

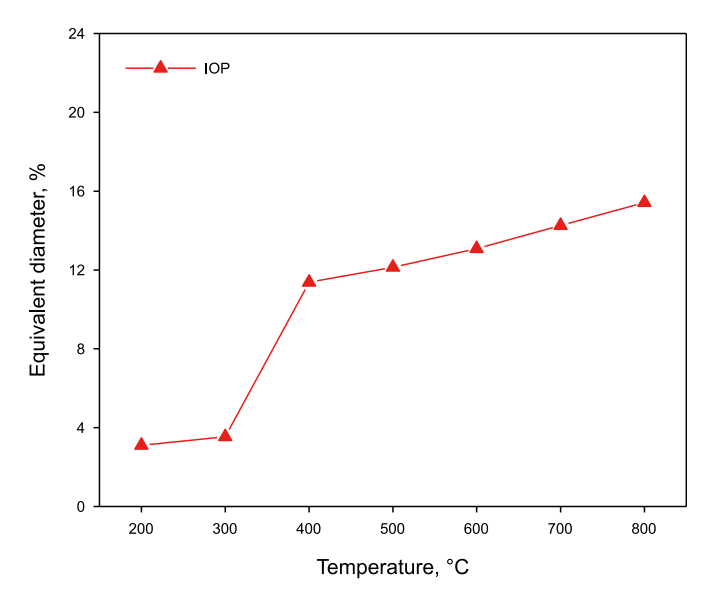


Fig. 7. Porosity changes of IOP.

#### approaches 3.

Fig. 9 shows the variation in the fractal dimension of the pores with the pyrolysis temperature of the organic-rich shale. Combined with the three-dimensional morphology of the pores obtained in Section 3.1.1, it can be found that the pores are initially mainly round. After 300 °C, owing to the pyrolysis of kerogen, many irregular pores develop in CK, and the fractal dimension increases. After the organic-rich shale has been pyrolyzed at 400 °C, the developed fractures connect with the pores in CK, significantly increasing the roughness of the pore structure. In addition, the spatial occupancy rate of the pores increases, and the connectivity is enhanced, which significantly enhances the range and flow ability of the high-temperature heating medium. Above 400 °C, the fractal dimension fluctuates around 2.62, indicating that the complexity of the pore surface of the organic-rich shale is relatively stable after pyrolysis at 400 °C.

This stability is important for assessing the storage capacity and fluid transport characteristics of organic-rich shale, as it can elucidate the potential impact of changes in the pore structure on the efficiency of oil and gas production at different pyrolysis stages.

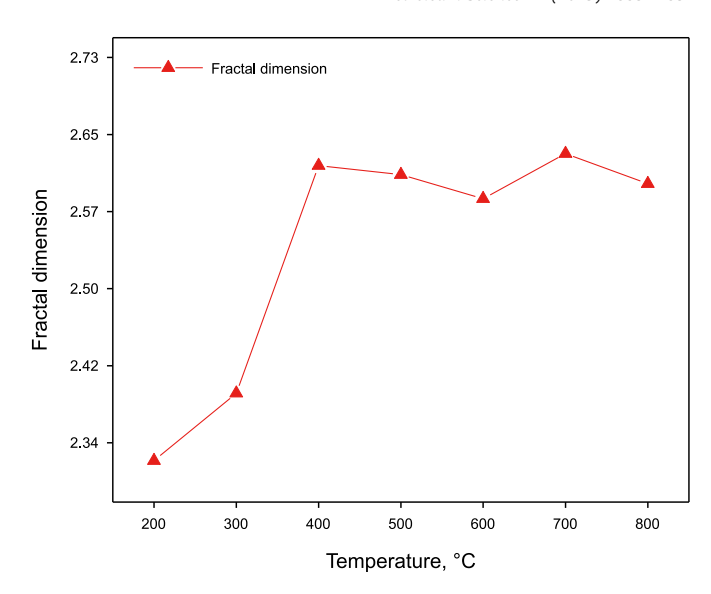


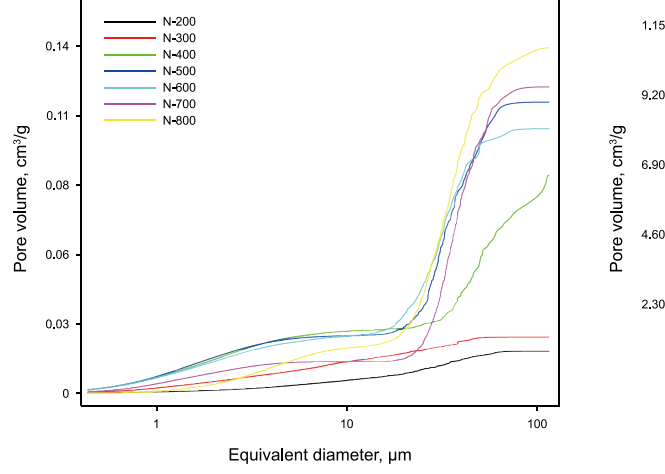
Fig. 9. Variation in the pore fractal dimension with pyrolysis temperature.

#### 3.2. CK and OP analysis

#### 3.2.1. Distribution of CK

In Section 2.4, the triphasic segmentation technique enabled the identification of CK within organic-rich shale through CT imaging. Using this approach, the distribution of CK during pyrolysis at various temperatures was determined, as illustrated in Fig. 10.

Fig. 10 shows localized threshold segmentation maps of the CK. At 200 °C, the organic-rich shale exhibits minimal development of primary pores, which are predominantly found within the CK. At 300 °C, the pyrolysis of kerogen, influenced by thermal stress, forms strip-like pores in the CK, indicating enhanced pore connectivity and increased permeability. With a further increase in temperature, images at 400 °C show the development of fractures along stratigraphic planes, connecting with flake-like pores within the CK. This results in increased permeability for high-temperature gases along the stratification direction and a marked enhancement in the mobility of kerogen pyrolysis products. At 500 °C, the decomposition of clay minerals initiates the collapse of the stratigraphic structure, producing a noticeable increase in the volume of pores in the CK. At 800 °C, the pyrolysis of carbonates results in a



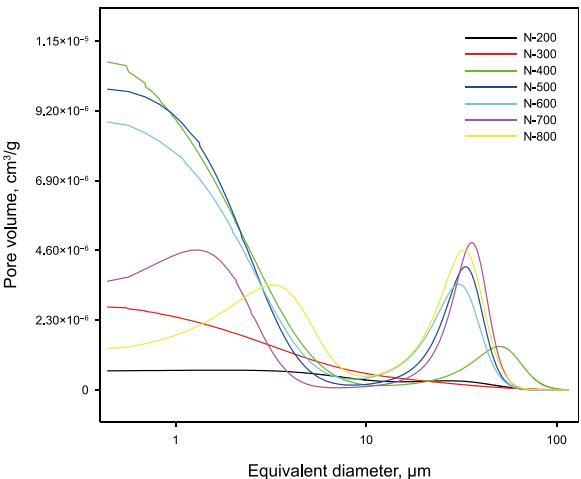


Fig. 8. Pore volume growth curves and pore size distribution of the IOP.

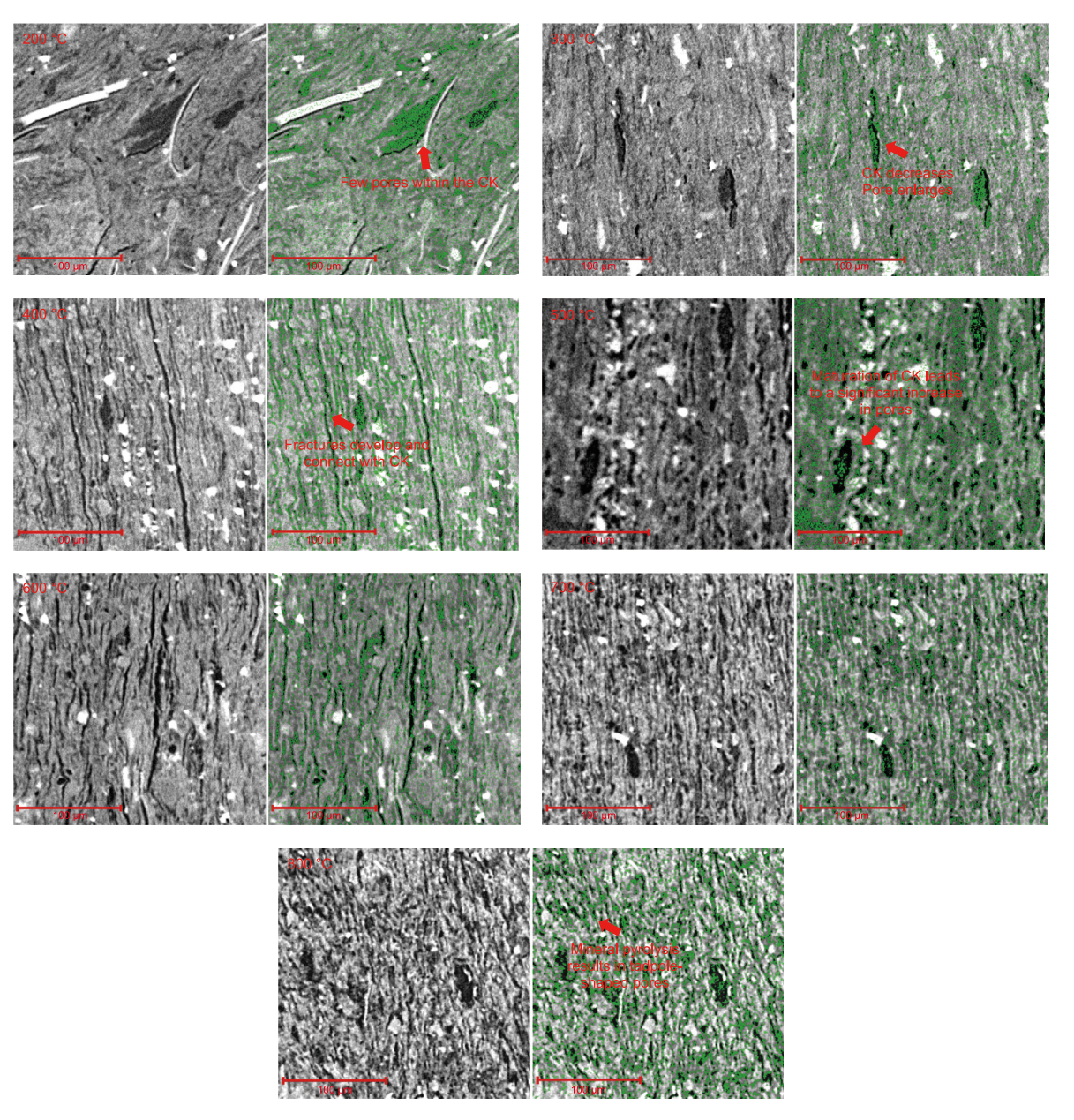


Fig. 10. Raw 2-D grayscale images and segmented image with CK shown in green.

reduction in the number of small pores, further expansion of existing pores, and the emergence of tadpole-shaped mineral dissolution pores.

#### 3.2.2. OP analysis

In traditional research, scholars have defined the visible pores within kerogen which can be detected by electron microscopy as organic pores. These pores exist at the nanoscale and are too small to be detected by even the most advanced CT technologies. Therefore, in previous studies, kerogen has often been regarded as a dense solid phase material, with the evolution of its internal pore structure being overlooked. This study innovatively proposes an analysis method for the internal organic pores of kerogen based on micro-nano CT technology.

Building on previous research, this study abstracts kerogen as a porous skeleton structure. Suekuni et al.'s research used helium pycnometry to quantify the changes in kerogen skeleton density with increasing maturity (Suekuni et al., 2022). The results showed

that as maturity increases, the internal skeleton density of kerogen gradually rises. In contrast, Vasileiadis et al.'s research indicated that as thermal maturity increases, the relative density of kerogen gradually decreases (Vasileiadis et al., 2017). These two research findings may seem contradictory, but they actually reflect different manifestations of the kerogen maturation process at different scales.

At the macro scale, the maturation of kerogen is marked by a decrease in both volume and relative density. This phenomenon occurs as oil progressively separates from the kerogen structure, resulting in an overall reduction in volume and a subsequent decline in relative density. Conversely, at the micro-scale, kerogen maturation is characterized by the separation of light components, the condensation of heavy components, and a notable increase in the density of the kerogen skeleton. During this process, the internal pore structure of kerogen undergoes complex changes, including the formation, expansion, contraction, and even disappearance of pores.

To comprehensively analyze the evolution of internal organic pores in kerogen, this study combines micro-nano CT technology with previous research findings. The specific operational steps are as follows.

 Established a linear relationship between image grayscale and density based on the principle that CT image grayscale is linearly related to relative density,

Vasileiadis et al. (2017) reported that the relative density of kerogen decreases as the pyrolysis temperature increases. This phenomenon can be observed in the CT images, where the gray gradient between the CK and IOM increases. To quantify this phenomenon, this study uses the principle that the X-ray absorption capacity of a substance varies with its density to analyze the relative density of kerogen based on the gray value of the CT images. Coshell et al. (1994) reported a robust positive linear correlation between CT values and volumetric density. Using this finding as a foundation, we adapted the CT analysis method typically used for bone density to acquire the average CT values for the specimen and CK using image-processing software. Employing Eq. (2), we established a relationship between the relative density of kerogen and the CT image grayscale. The results reveal how the relative density of kerogen varies with temperature. In Eq. (2), the ratio of the specimen density to the average CT value of the specimen represents a linear correlation between the density and CT value, and the relative density of kerogen is derived from the CT values of the CK. The results are summarized in Table 6. Fig. 11 shows the results in combination with the volumetric content of CK obtained in Section

$$\rho_{\rm ct} = \frac{\rho_{\rm s} \cdot H_{\rm k}}{H_{\rm s}} \tag{2}$$

In Eq. (2),  $\rho_{ct}$  is the relative density of CK, g/cm<sup>3</sup>;  $\rho_{s}$  is the specimen density, g/cm<sup>3</sup>;  $H_{k}$  is the CT value of CK; and  $H_{s}$  is the average CT value of the specimen.

The results indicate that the volume content of CK in the organic-rich shale gradually decreases with the progress of pyrolysis, and the main volume loss occurs between 300 and 400  $^{\circ}$ C. This suggests that the pyrolysis reactions of kerogen primarily occur between 300 and 400  $^{\circ}$ C. Furthermore, as the temperature increases, the oil and gas are volatilized, leading to a gradual decrease in the relative density of the kerogen. The pyrolysis of kerogen is a complex reaction accompanied by an increase in volume and a reduction in density.

(2) Correlate the maturity of kerogen in samples at different temperatures with the research results of Suekuni to obtain the skeletal density of kerogen.

Kerogen has a porous structure supported by an organic skeleton with internal pores that are mostly nanoscale micropores and mesopores (Shi et al., 2024). As the pyrolysis temperature increases,

**Table 6**CK relative density and related parameters.

Specimen	$H_{s}$	$P_{\rm s}$ , g/cm <sup>3</sup>	$H_{\mathrm{k}}$
N-200	4763.57	1.63	2815.55
N-300	9961.61	1.55	5825.56
N-400	4234.75	1.29	2025.10
N-500	12387.31	1.24	5991.90
N-600	12683.70	1.22	6307.68
N-700	7532.02	1.15	3707.69
N-800	3636.27	1.10	1790.56

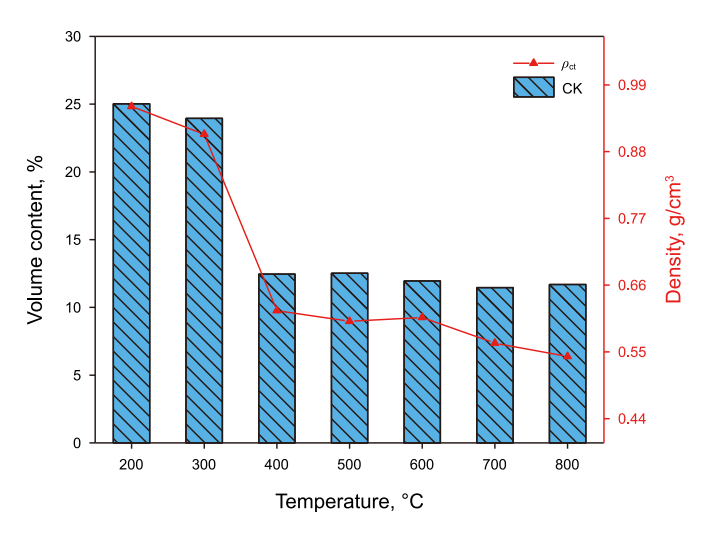


Fig. 11. Variations in the relative density and content of CK.

volatile light components are released, leaving behind the heavier components that constitute the skeleton, which ultimately remain as fixed carbon. Suekuni et al. (2022) identified the relationship between KS density and thermal maturity. Liu (2022) described the pattern of maturity in Huadian organic-rich shale with increasing pyrolysis temperature. Based on these studies, the KS densities of the specimens were obtained at different pyrolysis temperatures, as shown in Fig. 12.

(3) Calculate the organic pore content within kerogen by the difference between the relative density and skeleton density of the same volume of kerogen. The calculation method is shown in Eqs. (3) and (4).

$$\phi_{o} = \frac{V_{k} \cdot \rho_{ks} - V_{k} \cdot \rho_{ct}}{\rho_{ks} \cdot V_{s}}$$
(3)

$$Vg_{0} = \frac{\phi_{0}}{\rho_{c}} \tag{4}$$

where  $\rho_{ks}$  is the KS density of kerogen, g/cm<sup>3</sup>;  $\phi_0$  is the porosity of organic pores, %;  $V_k$  is the CK volume, cm<sup>3</sup>; and  $Vg_0$  is the OP volume, cm<sup>3</sup>/g.

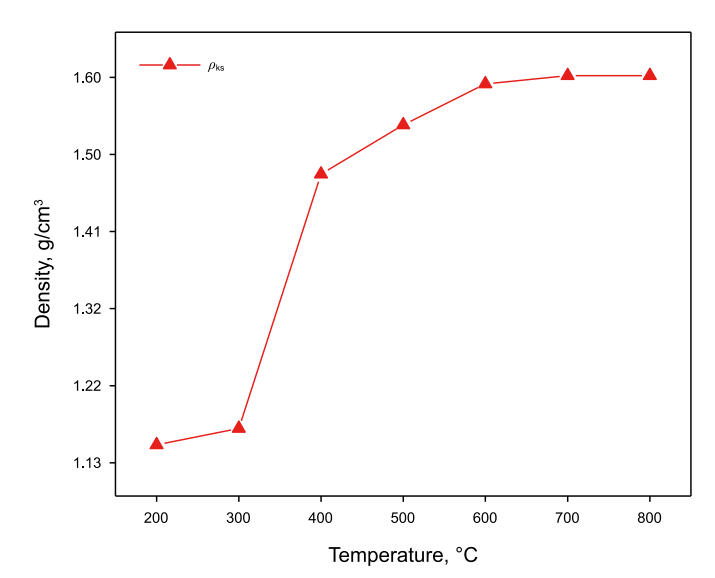


Fig. 12. Kerogen skeletal density with pyrolysis temperature.

Fig. 12 shows that at  $300-400\,^{\circ}\text{C}$ , the pyrolysis of heavy hydrocarbons leads to a rapid decrease in the volume and relative density of kerogen. As the thermal maturity increases, the skeletal density of the specimens increases rapidly, indicating that this stage is the main developmental phase for OP within the kerogen (Fig. 13). Above  $500\,^{\circ}\text{C}$ , as the pyrolysis of kerogen is completed, the OP porosity tends to become relatively stable. Above  $700\,^{\circ}\text{C}$ , a slight decrease in the relative density of kerogen is observed, which may be attributed to the reaction of  $CO_2$  produced from the pyrolysis of carbonate minerals with the internal carbon skeleton of the kerogen.

Incorporating the inorganic porosity from Section 3.1.1, the total pore content variation of the organic-rich shale during pyrolysis is predominantly governed by OP. When the temperature reaches 400 °C, the kerogen is sufficiently pyrolyzed, and oil and gas are volatilized, leading to the development of a significant number of organic pores within the kerogen. Additionally, owing to the aggregation of kerogen and the development of fractures, the IOP content increases and exceeds that of the OP, becoming the main part of the pore structure. Above 400 °C, the pyrolysis of kerogen concludes, and its internal structure becomes relatively stable. At this stage, the OP is fully developed, maintaining a porosity of approximately 7%-8%, which accounts for approximately 50% of the CK volume. Furthermore, owing to the development of fractures under thermal stress and the pyrolysis of inorganic minerals, the porosity of IOP gradually increases with the increasing pyrolysis temperature, reaching approximately 15% at 800 °C (Fig. 14).

#### 3.3. IOM and DK analysis

#### 3.3.1. Three-dimensional characterization of IOM

IOM, kerogen, and moisture are the main components of organic-rich shale; kerogen is the predominant form of organic matter, and the IOM has a complex composition. This study utilized micro-nano CT to explore the internal changes in the IOM of organic-rich shale, obtaining three-dimensional characterization images of the IOM (Fig. 15) and determining the changes in the IOM content (Fig. 16). It can be observed that during the pyrolysis process, the volumetric content of IOM changes little, and the minor variations are mainly due to specimen differences. Because of the limited precision of CT, it is impossible to accurately distinguish inorganic minerals and their three-dimensional structural pyrolysis mechanisms based on density differences. It is only possible to

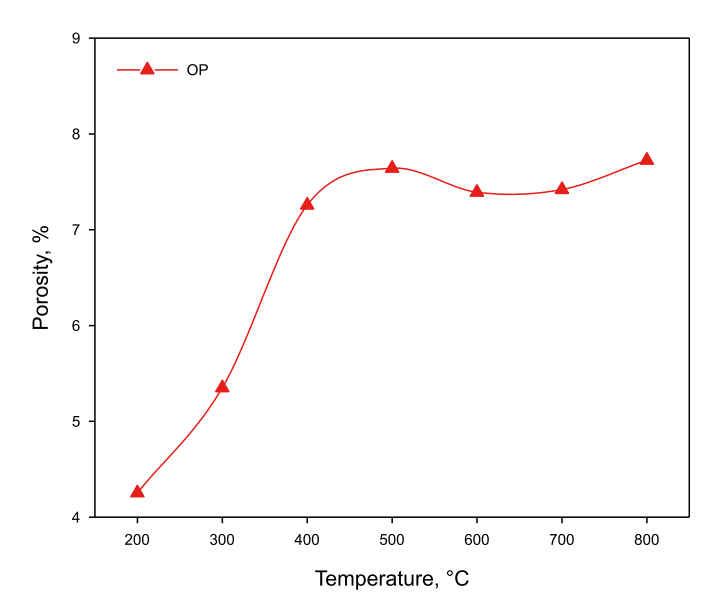


Fig. 13. Porosity variation of organic pores.

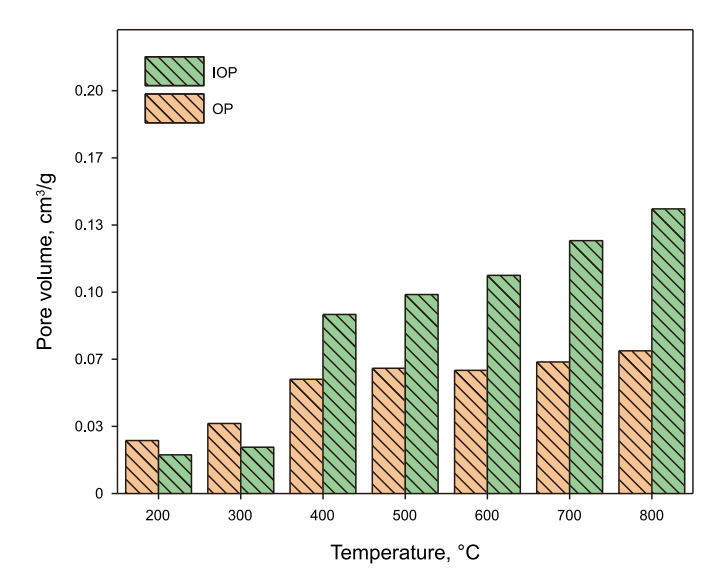


Fig. 14. Variation in the pore volume.

investigate the impact of inorganic mineral pyrolysis on the porosity by relating it to previous research and changes in the IOP (refer to Section 3.1.2).

By incorporating the results from rock pyrolysis experiments, it can be observed that the measured kerogen content exceeds the amount identified by the CT image analysis. This discrepancy suggests that CT image segmentation techniques cannot fully extract the total kerogen content of the specimens. Consequently, it is inferred that while a significant portion of the kerogen is present in clustered forms, a fraction of the kerogen is dispersed throughout the IOM.

#### 3.3.2. DK content analysis

Electron microscopy image Fig. 17 shows that there are a large number of clay minerals and kerogen interlayers inside the Huadian sample, and the thickness of these interlayers is much smaller than the detection accuracy of CT. According to the CT imaging principles (1. Each pixel represents the average density of that area; 2. High-density materials can interfere with X-rays), the grayscale of the kerogen/clay interlayers can be significantly higher than that of the CK, due to the significant differences in density characteristics between these mixed layers and CK. Similarly, in the CT images in Section 3.2.1 (Fig. 10), it is observed that the grayscale value in the area surrounding the CK is higher than that of the CK but lower than that of the IOM. We believe that this is a mixed layer of kerogen and IOM.

This detail, which has not been taken into account in previous studies, is crucial for accurately interpreting CT images and understanding the evolution of the kerogen.

To characterize the DK content in the kerogen/clay interlayers, the storage coefficient, *K*, is introduced to represent the mass ratio of DK to CK as follows:

$$K = \frac{M_{\rm k}/\rho_{\rm ct} - V_{\rm k}}{V_{\rm k}} \tag{5}$$

where *K* is the storage coefficient.

Fig. 18 shows the temperature-dependent variation in the storage coefficient for organic-rich shale. The results suggest that approximately 30% of the kerogen in Huadian organic-rich shale is present as DK within IOM. The plot indicates that with increasing pyrolysis temperature, the storage coefficient, *K*, tends to decrease, following a similar pattern to the kerogen content curve. This may

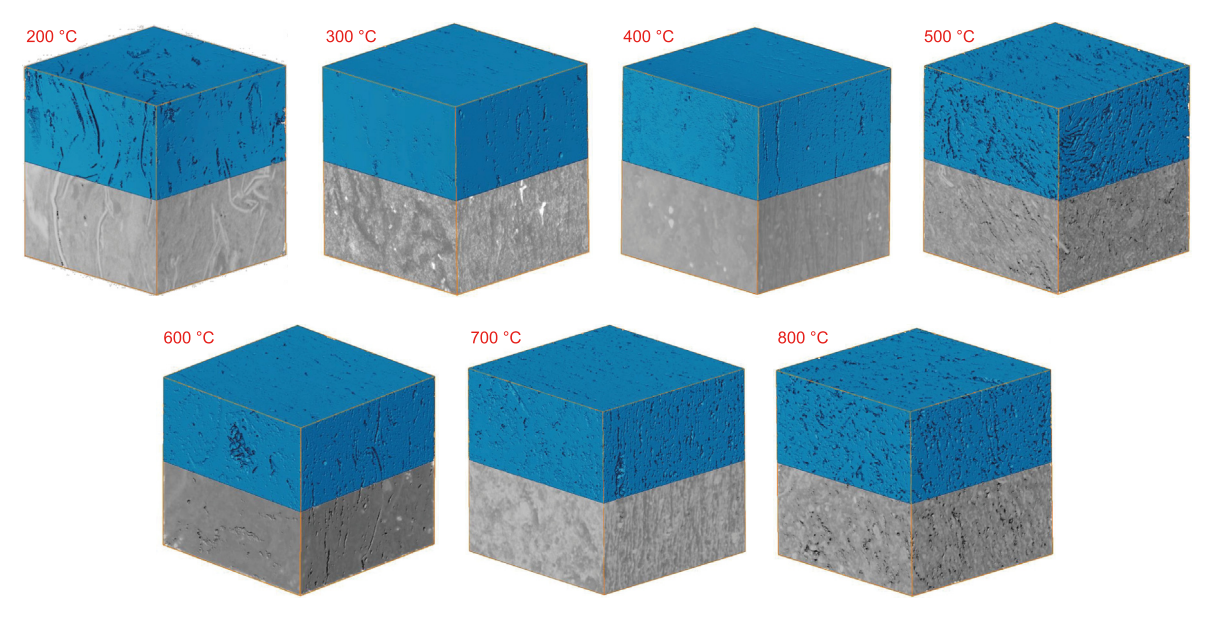


Fig. 15. 3-D volume rendered image with the IOM shown in blue (CT data dimensions:  $700 \times 700 \times 700$  pixels, with a pixel size of  $0.35 \, \mu m \times 0.35 \, \mu m \times 0.35 \, \mu m$ ).

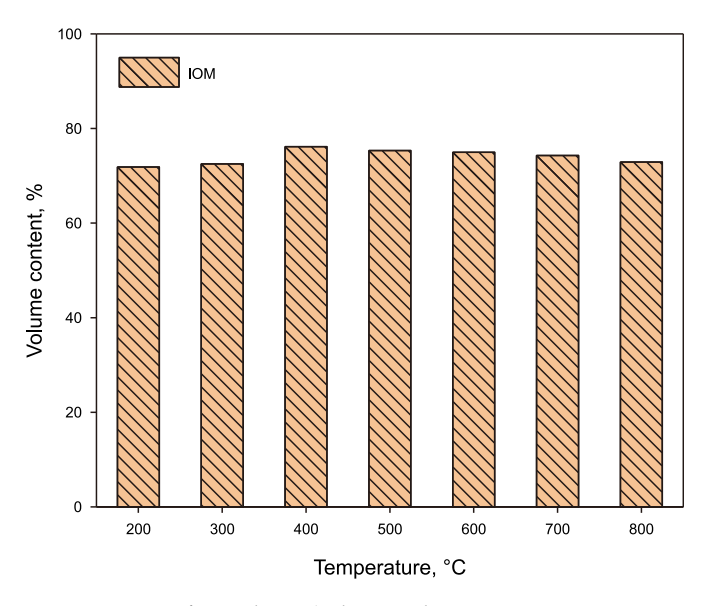


Fig. 16. Changes in the IOM volume content.

be due to the minor differences in the chemical composition of DK compared to CK, leading to a higher quality of oil and gas generated during pyrolysis.

Based on the above analysis, this study establishes a model for the distribution of kerogen and pores in organic-rich shales (Fig. 19) and its characterization method. Building on traditional three-phase segmentation, the kerogen within the organic-rich shale is divided into CK and DK, with pores categorized as inorganic and organic. CT can be used to measure CK and IOP directly. In contrast, OP and DK must be quantitatively obtained by combining rock pyrolysis analysis with the density of the KS. The volume content of each model part changes during pyrolysis, as shown in Fig. 20.

#### 4. Conclusion

In this study, high-resolution micro-nano CT scanning coupled with a triphasic segmentation approach is used to analyze the 3D

pore structure, kerogen distribution, and IOM in organic-rich shale specimens over a range of temperatures. By combining rock thermal decomposition and kerogen physicochemical characteristics, this study establishes the evolution of the organic and inorganic porosities of organic-rich shale with temperature. A considerable amount of DK is present within the IOM, and the pyrolytic behavior of CK and DK within the organic-rich shale is also elucidated. The principal results are summarized as follows.

- (1) The evolution of IOP during the pyrolysis process of organic-rich shale is divided into three stages. From 200 to 400 °C, the pyrolysis of kerogen generates a large number of pores, and fractures are produced along the weak stratigraphic planes due to thermal stress, causing the IOP porosity to increase from 3% to 11.4%. From 400 to 600 °C, thermal decomposition of clay minerals occurs, leading to the collapse of larger pores and a reduction in the layered structure. As a result, the content of smaller pores begins to decrease, and the IOP porosity increases from 11.4% to 13.1%. From 600 to 800 °C, the thermal decomposition of carbonate minerals causes a further reduction in smaller pores, with the IOP porosity reaching 15.4%.
- (2) The fractal dimension of IOP is relatively low at temperatures of 200–300 °C, indicating that at low temperatures, the IOP in organic-rich shale is primarily composed of pores with high circularity. At 300–400 °C, the fractal dimension rapidly increases and stabilizes at 400 °C, demonstrating that the roughness and connectivity of the inorganic pores are increased. This phenomenon is beneficial for expanding the reach of the high-temperature media and improving the heating efficiency of organic-rich shale reservoirs.
- (3) The mass loss of CK in organic-rich shale predominantly occurs at 300–400 °C, where the volumetric content decreases from 25% to 12.5%; it then remains relatively stable above 400 °C. The relative density of CK gradually decreases as the temperature increases from 9.5 to 5.4 g/cm³. Concurrently, the skeletal density of CK increases from 1.15 g/cm³ to 1.54 g/cm³ with increasing pyrolysis temperature. Predominantly, OP develops within the CK, achieving an OP porosity

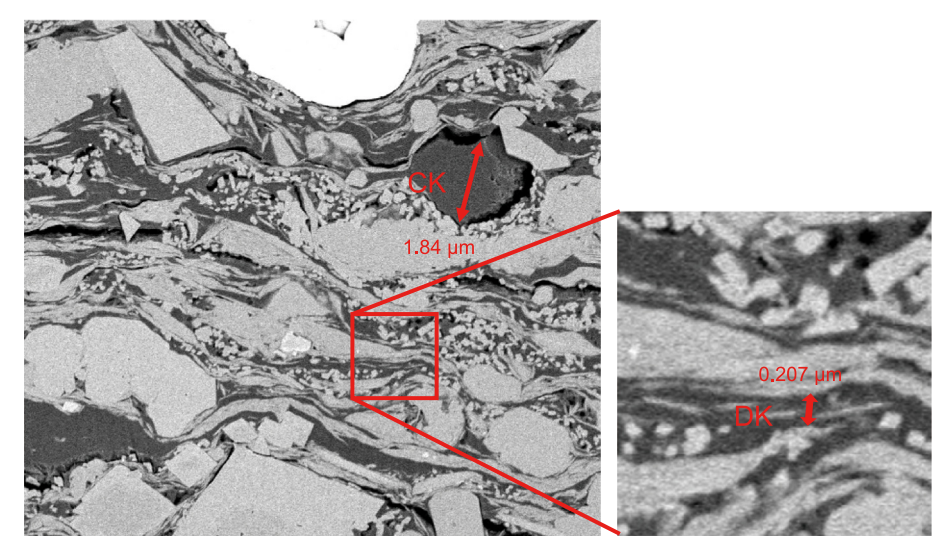


Fig. 17. High-resolution electron microscope image.

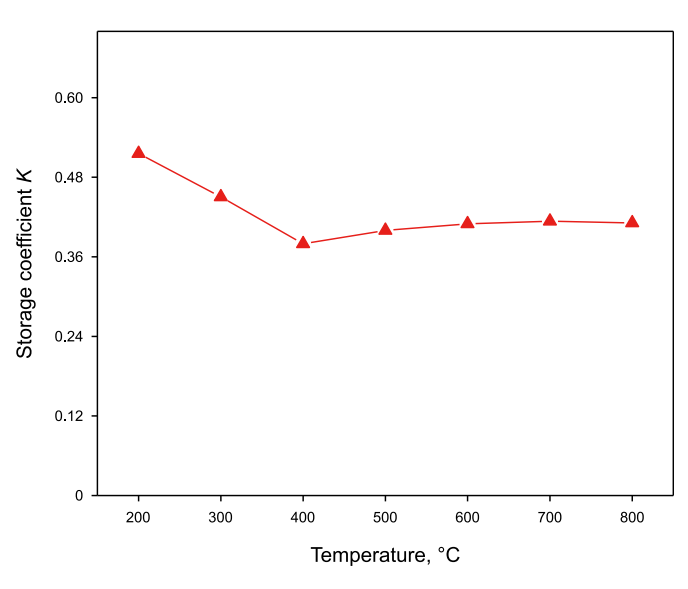


Fig. 18. Evolution of the storage coefficient with temperature.

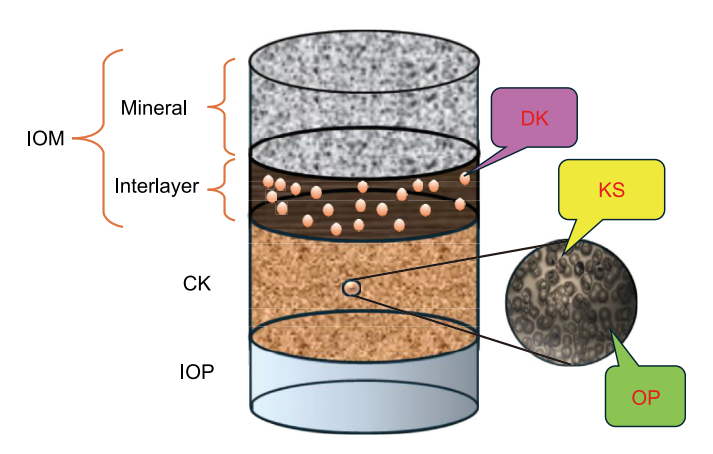


Fig. 19. Schematic diagram of the organic-rich shale model.

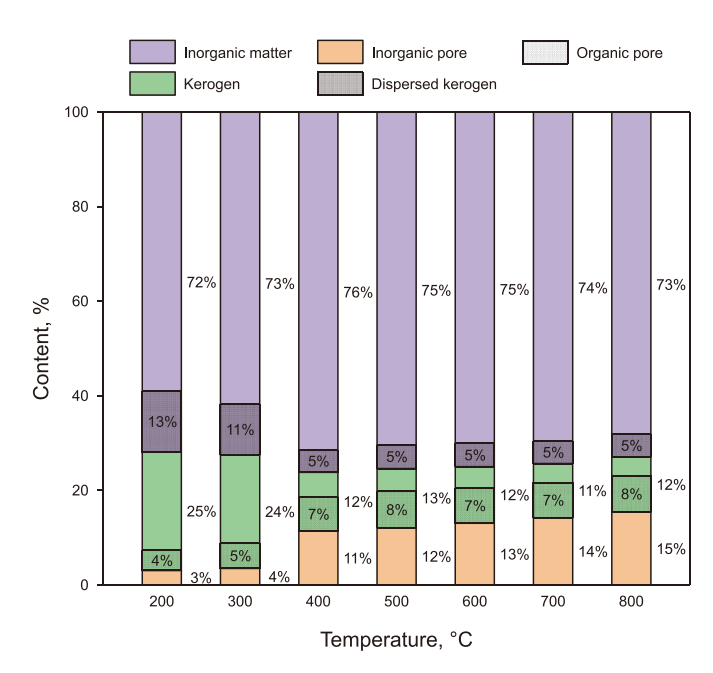


Fig. 20. Evolution of the volume content of organic-rich shale with temperature.

- of 7%—8% at 400  $^{\circ}\text{C}$  , which accounts for approximately 50% of the volume of CK.
- (4) Approximately 30% of the kerogen in organic-rich shale is present as DK within the IOM. The storage ratio, *K*, tends to decrease with increasing pyrolysis temperature, following a similar pattern to that of CK. It exhibits a decline between 200 and 400 °C and then stabilizes above 400 °C. The chemical composition of DK varies slightly from that of CK, leading to a somewhat higher quality of oil and gas generated during pyrolysis.

#### **CRediT authorship contribution statement**

**Chao-Fan Zhu:** Writing — review & editing, Supervision, Methodology, Conceptualization. **Tian-Le Zhang:** Writing —

original draft, Validation, Software, Investigation, Data curation. **Jun-Fan Pan:** Writing — review & editing, Validation. **Yan-Wei Li:** Writing — review & editing, Validation. **James J. Sheng:** Writing — review & editing, Validation. **Dong Ge:** Data curation, Software, Validation. **Rui Jia:** Supervision, Investigation, Data curation. **Wei Guo:** Writing — review & editing, Validation, Supervision, Investigation.

#### **Declaration of competing interest**

The authors declare that they have no known competing financial interests or personal relationships that could have appeared to influence the work reported in this paper.

#### **Acknowledgments**

We acknowledge the financial support offered by the National Oil Shale Exploitation R&D Center Open Fund Project (Grant No. 33550000-24-ZC0613-0055), National Key R&D Program of China (Grant No. 2019YFA0705502, Grant No. 2019YFA0705501), Science and technology research project of Education Department of Jilin Province (Grant No. JJKH20231185K) and the National Natural Science Fund project of China (Grant No. 4210020395, 51974334).

#### References

- Coshell, L., McIver, R.G., Chang, R., 1994. X-ray computed tomography of Australian oil shales: non-destructive visualization and density determination. Fuel 73 (8), 1317–1321. https://doi.org/10.1016/0016-2361(94)90307-7.
- Guo, W., Li, Q., Deng, S.H., Wang, Y., Zhu, C.F., 2023. Mechanism and reservoir simulation study of the autothermic pyrolysis in-situ conversion process for oil shale recovery. Pet. Sci. 20 (2), 1053–1067. https://doi.org/10.1016/ j.petsci.2022.08.030.
- Guo, W., Yang, Q.C., Deng, S.H., Li, Q., Sun, Y.H., Su, J.Z., Zhu, C.F., 2022. Experimental study of the autothermic pyrolysis in-situ conversion process (ATS) for oil shale recovery. Energy 258, 124878. https://doi.org/10.1016/j.energy.2022.124878.
- Han, X.X., Kulaots, I., Jiang, X.M., Suuberg, E.M., 2014. Review of oil shale semicoke and its combustion utilization. Fuel 126, 143–161. https://doi.org/10.1016/ i.fuel.2014.02.045.
- Hu, T., Pang, X.Q., Jiang, F.J., Zhang, C.X., Wu, G.Y., Hu, M.L., Jiang, L., Wang, Q.F., Xu, T.W., Hu, Y., Jiang, S., Wang, W.Y., Li, M.W., 2022. Dynamic continuous hydrocarbon accumulation (DCHA): existing theories and a new unified accumulation model. Earth Sci. Rev. 232. https://doi.org/10.1016/j.earscirev.2022.104109.
- Huang, X.D., Yang, D., Kang, Z.Q., 2021. Three-phase segmentation method for organic matter recognition in source rocks via CT images: a case study on oil shale pyrolyzed by steam. Energy Fuels 35 (12), 10075—10085. https://doi.org/ 10.1021/acs.energyfuels.1c00917.
- Kang, Z.Q., Zhao, J., Yang, D., Zhao, Y.S., Hu, Y.Q., 2017. Study of the evolution of micron-scale pore structure in oil shale at different temperatures. Oil Shale 34 (1), 42–54. https://doi.org/10.3176/oil.2017.1.03.
- Kang, Z.Q., Zhao, Y.S., Yang, D., 2020. Review of oil shale in-situ conversion technology. Appl. Energy 269. https://doi.org/10.1016/j.apenergy.2020.115121.
- Knaus, E., Killen, J., Biglarbigi, K., Crawford, P., 2010. An overview of oil shale resources. Oil shale: a solution to the liquid fuel dilemma. Am. Chem. Soc. 1032, 3–20. https://doi.org/10.1021/bk-2010-1032.ch001.
- Lei, J., Pan, B.Z., Guo, Y.H., Fan, Y.F., Xue, L.F., Deng, S.H., Zhang, L.H., Ruhan, A., 2021. A comprehensive analysis of the pyrolysis effects on oil shale pore structures at multiscale using different measurement methods. Energy 227. https://doi.org/ 10.1016/j.energy.2021.120359.
- Li, S.Q., Liu, Y.T., Xue, L., Zhu, D.D., 2022. Theoretical insight into the effect of polar organic molecules on heptane-water interfacial properties using molecular dynamic simulation. J. Petrol. Sci. Eng. 212. https://doi.org/10.1016/ j.petrol.2022.110259.
- Lin, C., He, J., Liu, Y., Mao, J., Li, X., Yang, X., Zhao, J., 2022. Quantitative characterization of cracking process in oil shale using micro-CT imaging. Arabian J. Geosci. 15 (3). https://doi.org/10.1007/s12517-021-09405-0.
- Liu, J.L., 2022. Evolution of Biomarkers in Lacustrine Rich Type I Organic Shale during Thermal Maturation and its Significance. Master Thesis. Central South University. https://doi.org/10.27661/d.cnki.gzhnu.2022.004132 (in Chinese).
- Liu, P., Kong, X., Feng, G.C., Zhang, K., Sun, S.Y., Yao, J., 2023. Three-dimensional simulation of wormhole propagation in fractured-vuggy carbonate rocks during acidization. Advances in Geo-Energy Research 7 (3), 199–210. https://doi.org/

10.46690/ager.2023.03.06.

- Liu, Z.J., Dong, Q.S., Ye, S.Q., Zhu, J.W., Guo, W., Li, D.C., Liu, R., Zhang, H.L., Du, J.F., 2006. The situation of oil shale resources in China. J. Jilin Univ. (Earth Sci. Ed.) (06), 869–876. https://doi.org/10.13278/j.cnki.jjuese.2006.06.001.
- Liu, Z.J., Liu, R., 2005. Oil shale resource state and evaluating system. Earth Sci. Front. (03), 315–323 (in Chinese).
- Lu, Q., Guo, J., Liu, Z., Ren, Y., Wang, X., Guan, B., Chen, C., He, L., 2023. Investigation of thermal induced damage of deep shale considering in-situ thermal shock effects. Geoenergy Sci. Eng. 222, 211439. https://doi.org/10.1016/j.geoen.2023.211439.
- Na, J.G., Im, C.H., Chung, S.H., Lee, K.B., 2012. Effect of oil shale retorting temperature on shale oil yield and properties. Fuel 95 (1), 131–135. https://doi.org/10.1016/ i.fuel.2011.11.029.
- Niu, M.T., Wang, S., Han, X.X., Jiang, X.M., 2013. Yield and characteristics of shale oil from the retorting of oil shale and fine oil-shale ash mixtures. Appl. Energy 111, 234–239. https://doi.org/10.1016/j.apenergy.2013.04.089.
- Qian, J.L., Wang, J.Q., Li, S.Y., 2006. World oil shale utilization and its future. J. Jilin Univ. (Earth Sci. Ed.) (06), 877–887. https://doi.org/10.13278/i.cnki.ijuese.2006.06.002.
- Rabbani, A., Baychev, T.G., Ayatollahi, S., Jivkov, A.P., 2017. Evolution of pore-scale morphology of oil shale during pyrolysis: a quantitative analysis. Transport Porous Media 119 (1), 143–162. https://doi.org/10.1007/s11242-017-0877-1.
- Saif, T., Lin, Q.Y., Butcher, A.R., Bijeljić, B., Blunt, M.J., 2017. Multi-scale multi-dimensional microstructure imaging of oil shale pyrolysis using X-ray microtomography, automated ultra-high resolution SEM, MAPS Mineralogy and FIB-SEM. Appl. Energy 202, 628–647. https://doi.org/10.1016/j.apenergy.2017.05.039.
- Saif, T., Lin, Q.Y., Gao, Y., Al-Khulaifi, Y., Marone, F., Hollis, D., Blunt, M.J., Bijeljic, B., 2019. 4D in situ synchrotron X-ray tomographic microscopy and laser-based heating study of oil shale pyrolysis. Appl. Energy 235, 1468–1475. https://doi.org/10.1016/j.apenergy.2018.11.044.
- Shi, K.Y., Chen, J.Q., Pang, X.Q., Jiang, F.J., Hui, S.S., Zhang, S.S., Pang, H., Wang, Y.Y., Chen, D., Yang, X.B., Li, B.Y., Pu, T.Y., 2024. Average molecular structure model of shale kerogen: experimental characterization, structural reconstruction, and pyrolysis analysis. Fuel 355, 129474. https://doi.org/10.1016/j.fuel.2023.129474.
- Suekuni, M.T., Craddock, P.R., Douglas, J.T., Pomerantz, A.E., Allgeier, A.M., 2022. Critical practices for the preparation and analysis of kerogen. Energy Fuels 36 (16), 8828–8843. https://doi.org/10.1021/acs.energyfuels.2c01063.
- Sun, B., 2013. Study on Mineral Decomposition Characteristics of Oil Shale. Master Thesis. Northeast Dianli University (in Chinese).
- Sun, Y.H., Bai, F.T., Liu, B.C., Liu, Y.M., Guo, M.Y., Guo, W., Wang, Q.W., Lü, X.S., Yang, F., Yang, Y., 2014. Characterization of the oil shale products derived via topochemical reaction method. Fuel 115, 338–346. https://doi.org/10.1016/j.fuel.2013.07.029.
- Tiwari, P., Deo, M., Lin, C.L., Miller, J.D., 2013. Characterization of oil shale pore structure before and after pyrolysis by using X-ray micro CT. Fuel 107, 547–554. https://doi.org/10.1016/j.fuel.2013.01.006.
- Vasileiadis, M., Peristeras, L.D., Papavasileiou, K.D., Economou, I.G., 2017. Modeling of bulk kerogen porosity: methods for control and characterization. Energy Fuels 31 (6), 6004–6018. https://doi.org/10.1021/acs.energyfuels.7b00626.
- Wang, Q., Sun, B., Liu, H.P., Bai, J.R., Xiao, G.H., 2013. Analysis of mineral behavior during pyrolysis of oil shale. J. Fuel Chem. Technol. 41 (2), 163–168 (in Chinese).
- Wang, S., Jiang, X.M., Han, X.X., Tong, J.H., 2012. Investigation of Chinese oil shale resources comprehensive utilization performance. Energy 42 (1), 224–232. https://doi.org/10.1016/j.energy.2012.03.066.
- Wang, Y.L., Liu, Z.J., Jing, H.L., Zhang, H.L., Zhang, J., 2005. Sedimentary characteristics of oil shale deposit of the huadian formation of paleogene in Huadian Basin. J. Jilin Univ. (Earth Sci. Ed.) (06), 42–46+53. https://doi.org/10.13278/j.cnki.jjuese.2005.06.007 (in Chinese).
- Xu, S.T., Sun, Y.H., Lü, X.S., Yang, Q.C., Li, Q., Wang, Z.D., Guo, M.Y., 2021. Effects of composition and pore evolution on thermophysical properties of Huadian oil shale in retorting and oxidizing pyrolysis. Fuel 305, 121565. https://doi.org/ 10.1016/j.fuel.2021.121565.
- Yang, Q.C., Guo, W., Xu, S.T., Zhu, C.F., 2023. The autothermic pyrolysis in-situ conversion process for oil shale recovery: effect of gas injection parameters. Energy 283, 129134. https://doi.org/10.1016/j.energy.2023.129134.
- Zhan, H.L., Yang, Q., Qin, F.K., Meng, Z.H., Chen, R., Miao, X.Y., Yue, W.Z., Zhao, K., 2022. Comprehensive preparation and multiscale characterization of kerogen in oil shale. Energy 252. https://doi.org/10.1016/j.energy.2022.124005.
- Zhao, J., Kang, Z.Q., 2020. Permeability of oil shale under in situ conditions: fushun oil shale (China) experimental case study. Nat. Resour. Res. 30 (1), 753–763. https://doi.org/10.1007/s11053-020-09717-0.
- Zou, C.N., Zhu, R.K., Wu, S.T., Yang, Z., Tao, S.Z., Yuan, X.J., Hou, L.H., Yang, H., Xu, C.C., Li, d. h., Bai, B., Wang, L., 2012. Types, characteristics, mechanisms and prospects of conventional and unconventional hydrocarbon accumulations: a case study of tight oil and tight gas in China. Acta Pet. Sin. 33 (2), 173—187 (in Chinese).
- Zou, S., Sun, C., 2020. X-ray microcomputed imaging of wettability characterization for multiphase flow in porous media: a review. Capillarity 3 (3), 36–44. https://doi.org/10.46690/capi.2020.03.01.